Optimized Stokes imaging for highly resolved optical speckle fields, Part II: optimal acquisition and estimation strategies

Jonathan Staes, Julien Fade

Optimized Stokes imaging for highly resolved optical speckle fields, part II: Optimal acquisition & estimation strategies

JONATHAN STAES,[1] AND JULIEN FADE[1,2,*]

[1] *Univ Rennes, CNRS, Institut FOTON - UMR 6082, F-35000 Rennes, France*
[2] *Aix-Marseille Univ, CNRS, Centrale Med, Institut Fresnel, Marseille, France*
[*] *julien.fade@fresnel.fr*

Abstract: In this second article of a three-paper series focusing on Stokes polarimetry of optical speckle fields resolved at the individual speckle grain scale, a theoretical study based on numerical simulations is presented in order to establish the optimum sensing, estimation and processing strategies that guarantee the best precision, accuracy and robustness for Stokes polarimetry in this specific context. In particular, it is demonstrated that the so-called State Of Polarization Analysis by Full Projection on the Poincaré space (SOPAFP) approach can be optimized in order to ensure best estimation performance. These numerical simulations also make it possible to establish that the SOPAFP approach provides better results in terms of robustness to residual experimental imperfections of the setup when compared to classical Stokes polarimetry approaches.

1. Introduction

This article is the second of a three-paper series titled "Optimized Stokes imaging for highly resolved optical speckle fields". In the first article of the series [1], we have extensively described an optimized experimental Stokes polarimetric imaging system resolved at the speckle grain scale, and shown some preliminary results validating the experimental setup. In this second article, we will rely on numerical simulations to investigate and establish the optimal sensing and estimation strategies to perform Stokes imaging in the context of highly resolved speckle pattern.

For that purpose, we will compare the performances of various estimation schemes for (full-Stokes) polarimetry:

- either with approaches commonly used in standard polarimetric imaging involving a limited number (≥ 4) of intensity measurements along different polarization analyzing directions;
- or with the so-called SOPAFP approach (State Of Polarization Analysis by Full Projection on the Poincaré space) proposed initially in [2], and which, as its name suggests, probes numerous (several 10's to several 100's) polarimetric states located at the surface of the Poincaré sphere.

These various approaches and the optimal choice for these probe states are discussed in Section 3, after Section 2 recalls the mathematical formalism required. In Section 4, based on numerical simulations of realistic experiments, we evidence (for the first time to our knowledge) the fundamental interest of the SOPAFP approach by showing how it allows to guarantee the highest estimation accuracy and precision independently of the signal-to-noise (SNR) level or the degree of polarization (DOP) of light, while superseding classical approaches in terms of robustness or unbiasedness to certain experimental imperfections (such as calibration defects, misalignments,...). These comparisons are based on numerical simulations to evaluate various experimental influences encountered when studying the speckle field in a highly resolved manner. Indeed, the influence of SNR, orientation error and polarimetric analyzer calibration error on the quality of estimation of the state of polarization is evaluated, as is the ability of each approach to estimate partially depolarized states.

2. Mathematical formalism and notations

Throughout this paper, we will rely on the so-called Mueller/Stokes formalism to describe the polarimetric light-matter (linear) interaction by matrix calculation. The polarimetric state $\mathbf{S}^{out}$ resulting from the interaction of an incident polarization state $\mathbf{S}^{in}$ with a given sample can be calculated as follows [3] as $\mathbf{S}^{out} = M\,\mathbf{S}^{in}$, where M denotes a real 4×4 Mueller matrix which characterizes the polarimetric response of the sample. In the above equation, $\mathbf{S}^{in}$ (respectively $\mathbf{S}^{out}$) denotes the Stokes vector (4-component real, column vector) of the input (resp. output light). This Stokes formalism is widely used in polarimetric imaging due to its ability to describe any polarimetric state of a light source, whether the light is fully polarized or not, and to the accessibility of its parameters through experimental intensity measurements. It is therefore perfectly suited for polarimetric imaging of highly resolved speckle fields and is classically defined [4] as $\mathbf{S} = \left[S_0,\ S_1,\ S_2,\ S_3\right]^T$, where $.^T$ denotes matrix transposition and with $S_0 = E_{0x}^2 + E_{0y}^2$, $S_1 = E_{0x}^2 - E_{0y}^2$, $S_2 = E_{0x}^2 E_{0y}^2 \cos(\phi)$ and $S_3 = E_{0x}^2 E_{0y}^2 \sin(\phi)$, E_{0x} (respectively E_{0y}) denoting the horizontal (respectively vertical) component of the transverse electric field of the light. S_0 represents the total intensity, S_1 is the portion of light linearly polarized along the vertical or horizontal axis, S_2 is the portion linearly polarized along the $\pm 45°$ axes and S_3 represents the portion circularly polarized right or left [4]. The degree of polarization can be determined from the Stokes vector as follows:

$$DOP = \frac{\sqrt{S_1^2 + S_2^2 + S_3^2}}{S_0} = \sqrt{s_1^2 + s_2^2 + s_3^2} = \|\mathbf{s}\|\,, \tag{1}$$

where the $s_i = S_i/S_0$, $_{i=1,\ldots,3}$ are the components of the reduced 3-dimensional Stokes vector $\mathbf{s}$ and with $\|.\|$ denoting the vector quadratic norm.

Experimental estimation of the full Stokes vector therefore requires a minimum of four intensity measurements I_k resulting from the projection of the incident state S^{in} with the probed polarimetric state $\mathbf{S}_{PSA,k}$ where k represents the index of the probed state of the polarimetric analyzer. The intensity measured for each acquisition of index k results from a scalar product of the input Stokes vector with the analysis Stokes vector, as $I_k = \mathbf{S}_{PSA,k}^T.\mathbf{S}^{in}$. More generally, the set of measured intensities $\mathbf{I}$ can be written as a k-dimensional column vector: $\mathbf{I} = [I_1, \cdots, I_k, \cdots, I_N]^T = W\,\mathbf{S}^{in}$ where W represents the *analysis* matrix composed of N probe states $\mathbf{S}_{PSA,k}$ ($k \in [1, N]$). The matrix can be defined through the following equation: $W^T = \left[\mathbf{S}_{PSA,1} \ldots \mathbf{S}_{PSA,N}\right]$.

The concept of estimating the polarization state using a Mueller matrix description of the polarization state analyzer is not new and has provided a rich (both theoretical and experimental) literature even recently with non standard approaches [5–7]. Thus, to estimate the Stokes vector for a single polarization state, there exists a variety of available W sensing matrices. The selection of this analysis matrix depends mainly on the experimental conditions, such as the accessibility of the probe states and the number of states to be probed as a function of the available time to perform the measurement. Some probe states are more easily accessible with conventional optical elements, but the use of a variable delay phase plates such as liquid-crystal variable retarders (LCVRs) now makes it possible to access to any probe state. Indeed, as extensively described in the Part I of this article series [1], using a pair of LCVRs with appropriate orientations, followed by a polarizer, it is possible to access any probe state across the Poincaré's sphere, by addressing the LCVR1 (respectively LCVR2) with voltage level V_1 (resp. V_2), inducing an optical phase delay ϕ_1 (resp. ϕ_2) which is deduced from V_1 from a calibration step performed at fixed temperature and given wavelength. It is important to notice that, troughout this article series, experiments and simulations were performed at a fixed monochromatic wavelength of $\lambda = 532$ nm. Non-monochromatic illuminations could also be envisaged, but would require accounting for the dispersion of the optical elements and the optical phase delay of LCVRs. The

optimal choice of the W analysis matrix is discussed in more details in next section.

3. Analysis matrices W and associated estimation methods

This section describes the classical polarization analysis states (or equivalently, the analysis matrices W) commonly used in polarimetric imaging and the associated estimation approaches. The most widely used sets of polarization analysis states will be referred here as *Stokes-4* (abbreviated *St-4*) and *Stokes-6* (abbr. *St-6*), and are represented respectively on the top left and top right corners of Fig. 1. The bottom left corner of Fig. 1 shows the classical *Tetrahedron* (abbr. *Tet*) analysis matrix for which optimality results for the estimation performance under various noise models hold [8–14]. The last set of polarization analysis states, represented in the bottom right part of Fig. 1, and which will be referred to as *Spiral* (abbr. *Sp*), is much less widespread in the polarimetric imaging community. However, it has shown great experimental interest for polarimetric imaging of highly resolved speckle fields [15], and is at the core of the so-called SOPAFP approach described above.

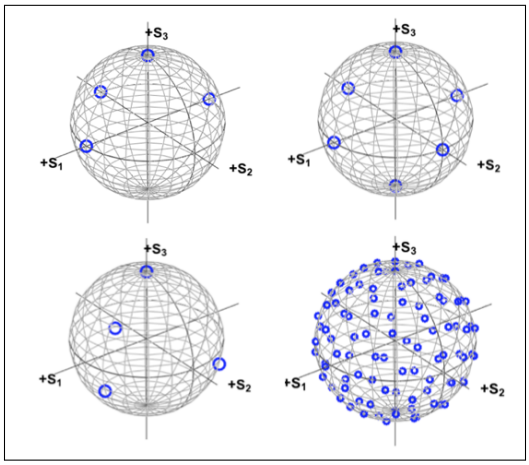

Fig. 1. Poincaré's sphere representation of various sets of polarization analysis states used in Stokes polarimetric imaging: (top left) *Stokes-4*, (top right) *Stokes-6*, (bottom left) *Tetrahedron* and (bottom right) *Spiral*.

All of these approaches are based on the measurement of a set of intensity values, related to the incident polarimetric state by a system of linear equations recalled above. The performance of the various sets of analysis states (i.e., of matrices W) in solving such system is studied in the following sections, in terms of estimation accuracy and precision, as well as robustness to experimental imperfections. For this purpose, we need to introduce the condition number (CN) of an analysis matrix W, defined as $CN(W) = \|W\| \cdot \left\|W^{-1}\right\|$ [16], where $\|.\|$ denotes the Euclidian matrix norm. In this case, this CN is equal to the ratio between the largest and the smallest singular value of the matrix W. In dimension 4, for the mathematical space of the Stokes vectors, it is well known that its optimal value is $\sqrt{3}$ ($\simeq 1.7321$) [11].

3.1. Stokes-4

The *Stokes-4* acquisition analysis matrix enables all these parameters to be evaluated in a minimum of four measurements. Typically, the four intensities measured are I_H, I_V ,I_{+45} and I_L, corresponding to analyzing the light through standard directions of polarizations. These intensities are easily accessible with conventional optical elements (polarizer, quarter-wave phase plate, etc.), and correspond to the linear probe states (horizontal, vertical and +45°) and the

circular probe state (circular left in our case). The resulting conditioning number is not optimal and is equal to 3.226. With this configuration, the estimates of the incident Stokes vector are generally obtained directly through:

$$\widehat{\mathbf{S}}_{St\text{-}4} = \begin{cases} S_0 = I_H + I_V \\ S_1 = I_H - I_V \\ S_2 = 2 \cdot I_{+45} - S_0 \\ S_3 = 2 \cdot I_L - S_0 \end{cases} \tag{2}$$

where $\widehat{\mathbf{S}}_{St\text{-}4}$ represents the estimated Stokes vector.

3.2. Stokes-6

The *Stokes-6* analysis matrix is used to determine the Stokes vector from the following six intensity measurements: I_H, I_V ,I_{+45} ,I_{-45}, I_G and I_D. These intensities correspond to the six probe states: horizontal, vertical, $\pm 45^\circ$ and circular left and right. They are easily accessible experimentally, as described above. However, since this analysis matrix forms a regular octahedron within the Poincaré sphere (platonic solid), it allows an optimal CN equal to $\sqrt{3}$ to be obtained. The incident Stokes vector is also estimated by a direct computation of:

$$\widehat{\mathbf{S}}_{St\text{-}6} = \begin{cases} S_0 = I_H + I_V \\ S_1 = I_H - I_V \\ S_2 = I_{+45} - I_{-45} \\ S_3 = I_L - I_R \end{cases} \tag{3}$$

3.3. Tetrahedron

With technological advances, and in particular owing to the democratization of variable delay LCVRs, it has become possible to choose the polarization analysis states at will across the Poincaré's sphere. As a result, it is well-established that the optimum CN is obtained with minimum of 4 measurements when these states are located on the summits of a regular tetrahedron [8–14]. The incident Stokes vector is in that case estimated by a direct inversion of the analysis matrix W (full-rank) as follows:

$$\widehat{\mathbf{S}} = W^{-1}\mathbf{I} \tag{4}$$

3.4. SOPAFP approaches

An alternative introduced as SOPAFP (State Of Polarization Analysis by Full Projection on the Poincaré space) was implemented for the first time by J. Dupont *et al.* in the context of Stokes imaging of highly resolved speckle grains [2, 15]. It consists in probing an important number N of polarimetric states uniformly distributed across the surface of the Poincaré's sphere. This approach makes it possible to acquire finer polarimetric results than previous approaches, particularly in low-intensity areas, at the expense of a longer acquisition time. In this seminal work, the distribution of the analysis states formed a spiral across the Poincaré's sphere, and we shall refer to this set as "*Spiral*".

3.4.1. Spiral

The set of states used in [15] were chosen so as to form a spiral winding around the S_3 axis (see bottom right of Fig. 1). In this work, the Stokes vector was estimated at each pixel of the CCD

sensor by using a non-linear regression [2, 15] applied to an intensity curve obtained at each pixel of the sensor. Indeed, when the various sensing states are applied successively, the measured intensity at each pixel describes a curve as a function of the polarization state probed, and the shape of the curve unequivocally correspond to a given input state. An example of such curve is shown in Fig. 6 of the first article of this series [1], for a spiral composed of $N = 96$ states, providing a CN of $1.742 > \sqrt{3}$, but close to the optimal value.

This approach, coupled to a non-linear regression estimation technique, was applied to the experimental bench in our laboratory and has been tested in this work on simulation results in order to compare the performance with other estimation approaches. In our implementation, a non-linear regression was applied to each intensity curve to estimate the parameters p, χ and ψ corresponding respectively to the DOP, the polarization ellipticity and the polarization azimuth of the input light polarization , at a given pixel. These estimated parameters were finally used to derive the incident reduced Stokes vector, described in spherical coordinates as $\mathbf{s}_{in}^T = \left[s_1\ s_2\ s_3\right]^T$, with $s_1 = p\ \cos(2\psi)\cos(2\chi)$, $s_2 = p\ \sin(2\psi)\cos(2\chi)$ and $s_3 = p\ \sin(2\chi)$.

We can note that this approach is similar to that used by Dupont, *et al.* in [2, 15], except that they relied on a different parameterization of the input Stokes vector. In our case, the intensity measured by the CCD sensor can be rewritten as a function of the three parameters p, χ and ψ of the incident Stokes vector and of the optical delays ϕ_1, k and ϕ_2, k introduced by the LCVR1 and LCVR2 plates for each state $k = 1, \ldots, N$ to be analyzed as:

$$\begin{aligned} I_k = \frac{I_0}{2}\big[1 &- p \cdot \cos(2\chi)\cos(2\psi)\cos(\phi_{2,k}) \\ &- p \cdot \sin(2\chi)\cos(\phi_{1,k})\sin(\phi_{2,k}) \\ &+ p \cdot \cos(2\chi)\sin(2\psi)\sin(\phi_{1,k})\sin(\phi_{2,k})\big], \end{aligned} \tag{5}$$

with I_0 the total intensity of the input state. As described in Section 4, this equation has been used in the present work to simulate the intensity measurements (direct model).

On the other hand, to evaluate the Stokes vector at each pixel from the measured intensity vector, we used an optimization algorithm (implemented on GNU Octave using the function fminsearch() [17]), to determine the parameters p, χ and ψ, given that the values of ϕ_1, k and ϕ_2, k are in principle perfectly known and correspond to the optical phase delays introduced by the LCVRs if the system is properly calibrated. The criterion to minimize simply consisted in a root-mean-square (RMS) error, defined as :

$$\hat{\epsilon}(p, \chi, \psi) = \sum_{k=1}^{N} |I_{simul,k}(p, \chi, \psi, \phi_{1,k}, \phi_{2,k}) - I_k|^2 \tag{6}$$

This optimization algorithm, which is based on the Nelder-Maed's [18] method, requires an approximate knowledge of the values of the parameters to be determined (initialization values) to prevent the optimisation of the algorithm from converging to a local minimum. To satisfy this requirement, an intensity look-up-table (LUT) has been generated for the phase shifts $\phi_{1,k}$ and $\phi_{2,k}$ by varying each parameter p, χ and ψ from 0 to 1 in steps of 0.1. In this way, 1331 intensity curves were simulated in the LUT, allowing the initialization value of the parameters vector in the optimization algorithm to be determined by picking up the set of parameters that minimizes the RMS residual error described by (6) between the measured intensity curve and the 1331 tabulated curves. Once seeded with such initialization, the minimization algorithm was shown to converge easily towards an estimated value. An example of a result obtained is shown in Fig. 6 of the first paper of this series [1], where we simulated the intensity curve that would be obtained by illuminating a metal plate with a light source with left circular incident polarization, and analyzing the backscattered light through $N = 96$ *spiral* analysis states. The

curve I_{th} corresponds to the theoretical polarization input state, whereas I_{opt} stands for the intensity variation obtained with the parameters estimated by numerical optimization.

However, in an imaging context, this optimization must be carried out at each location (pixel) of the image, which requires significant post-processing time for images of the order of 700×700 pixels. For example, with a 4x4 pixel binning factor, the post-processing time lasts about $5.3 \times 10^3 s$, i.e. almost 90 minutes on an ordinary computer. To minimize this processing time, we proposed to rely on a classical direct inversion scheme, involving the pseudo-inverse of W, since in this case W is not an invertible square matrix anymore, i.e.,

$$\widehat{\mathbf{S}}_{Sp} = (W^T W)^{-1} W^T \mathbf{I}. \tag{7}$$

As shown below, such inversion improves the processing time by several orders of magnitude.

3.4.2. Spiral of tetrahedrons analyzing states

As stated in the previous subsection, for $N = 96$ states probed, the *Spiral* analysis matrix is close to the optimum CN, but it has the disadvantage that this CN depends on the number of states probed (see Fig. 2.b). By optimizing the location of the polarization probe states, it is possible to ensure that the CN of the selected matrix W is strictly equal to $\sqrt{3}$. For that purpose, we propose to use a set of analysis states, referred to as *Spiral of tetrahedrons* (abbr. *SpTet*), which consists of a set of N_T regular tetrahedrons inscribed in the Poincaré's sphere, providing $N = 4\,N_T$ probe states (i.e., a $4 \times N$ analysis matrix). As a result it is possible to build a set of states with optimum CN of any size N, provided N is a multiple of 4. An example of such set of states is provided in Fig. 2.a: $N = 96$ states have been generated from $N_T = 24$ tetrahedrons using the following method (detailed in Supplemental Information 1): starting with a first reference tetrahedron, regular rotations are applied so that one of the vertices of the tetrahedrons follows the trajectory of a spiral wounded along the S3 axis (blue markers in Fig. 2.a) according to the previous *Spiral* approach. However, this rotation does not modify all four vertices in the same way, producing a less uniform distribution on the surface of the Poincaré's sphere, and the procedure detailed in Supplemental Information 1 is used to warrant the maximal uniformity of the N probe states accross the sphere.

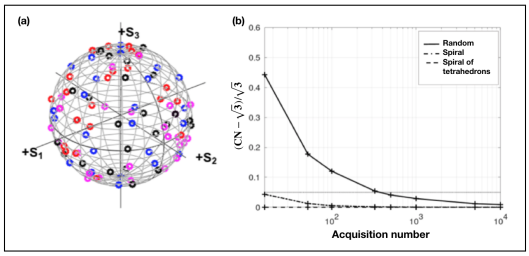

Fig. 2. (a) Distribution of analysis states for the *Spiral of tetrahedrons* analysis matrix, where each colour represents the state resulting from the rotation of one of the vertices of the reference tetrahedron. (b) Evolution of the CN of three analysis matrices (*Spiral of tetrahedrons*, *Spiral*, and uniformly distributed random set of points) as a function of the number of states $N \in \{16, 52, 100, 324, 500, 1000, 5000, 10000\}$.

In Fig. 2.b, we represented the relative excess in CN, with respect to the minimum optimal value of $\sqrt{3}$, for three different sets of probe states with increasing number of points $N \in \{16, 52, 100, 324, 500, 1000, 5000, 10000\}$: the *Spiral of tetrahedrons* set, the *Spiral* set, and a uniformly distributed random set of states. This plot confirms that, by construction, the *Spiral of tetrahedrons* set maintains optimal CN of the matrix W independently of the number of probe states. The conditioning of the "Spiral" matrix is very close to the optimal value when the number

of probe states is above 100. Finally, the CN obtained with the random set is very dependent on the number of states and increases very rapidly when the number of probe states decreases.

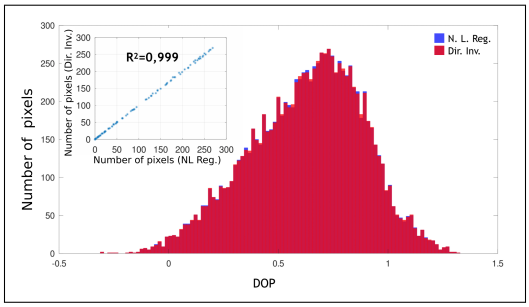

Fig. 3. Example of histogram of the DOP estimated by non-linear regression (blue) or direct inversion (red) on an experimental speckle image of 10^4 pixels. Inset: The number of pixels in each class obtained by the direct inversion method is plotted against those obtained by non-linear regression.

To conclude this section, we provide a comparison between the estimation results obtained on experimental data by the non-linear regression approach (as used in anterior implementations of the SOPAFP method [2, 15]), and by the direct inversion procedure of Eq. (7) in order to validate that this latter approach is able to provide the same results but with a huge acceleration in processing time. In Fig. 3, we plotted the histogram of the DOP values estimated on 10^4 pixels of a speckle image obtained by illuminating a metal plate with a vertically polarized incident homogeneous light beam. The experimental setup corresponds to the one described in the first part of this article series [1]. This graph shows that the two estimation methods are very similar, which is confirmed by the coefficient of determination R^2 of 0.999. Across the whole field of view of 700×700 pixels accessible in this experiment, using a binning factor of 2×2, the non-linear regression estimation requires $> 2 \times 10^4$ s, whereas only 14.4 s are required for direct inversion, i.e., an speed-up factor of more than 1500 times. In the following of this article series, direct inversion estimation will then be used when the SOPAFP approach is implemented, and in particular in the simulation results presented in the next section.

4. Comparative performances of analysis matrices for Stokes imaging

In this section, we describe the methodology and performance metrics used to generate exhaustive simulations of the estimation performances (in terms of accuracy and precision) of the various sensing strategies detailed above. We then comparatively analyze the efficiency of these various matrices W while varying the simulated experimental conditions in terms of signal-to-noise ratio (SNR), DOP and influence of an imperfect calibration/alignment of the experimental setup.

4.1. Simulation methodology

The five choices of analysis matrices W presented above will be compared in this section in terms of Stokes vector estimation performance. To compare these various sensing approaches on a fair basis, we will consider a set of $N = 96$ simulated experimental measurements for each matrix W. For all matrices W requiring fewer analysis states, we will consider a repetition of independent measurements in order to obtain the same number of $N = 96$ intensity measurements, as summarized in Table 1.

Now, in order to characterize the "average" estimation performance of each analysis matrix W over all the input polarimetric states $\mathbf{S}_{in}$ that could be encountered, we further simulated $M = 10^3$ randomly selected input Stokes vectors. These randomly simulated states were in practice

Table 1. **Comparison between the number of analysis and repetition states for each analysis matrix.**

Matrix W	Stokes 4	Stokes 6	Tetrahedron	Spiral	Spiral of tetrahedrons
# distinct states	4	6	4	96	96
# repetitions	24	16	24	1	1
Total measures	$N = 96$				

produced so as to obtain Stokes vectors corresponding to a purely polarized light ($DOP = 1$), by drawing $M = 10^3$ independent uniformly distributed values between -1 and 1 of the three reduced Stokes parameters s_1, s_2 and s_3. After normalization of the vector $\mathbf{s}_{in}$, and multiplication by a constant value S_0, we obtain the set of simulated Stokes vectors as: $S_{in}^T = S_0 \left[1 \quad \frac{\mathbf{s_{in}}^T}{\|\mathbf{s_{in}}\|}\right]$.

Finally, we modeled the influence of the photon noise on the simulated acquisitions. This is important as, in the context of speckle imaging at the grain scale, the acquired intensity images are composed of bright grains (corresponding to constructive interferences) and dark areas (corresponding to destructive interferences). The SNR is therefore higher in the bright areas, while it is degraded in the regions of lower intensity. The SNR therefore varies spatially in the intensity image, and we must verify the robustness of the estimation procedure w.r.t. noise. For that purpose, all measurements were repeated over a number of $R = 10^3$ independent realizations of Poisson noise affecting the intensity measurement simulated. For each simulated acquisition with average intensity I, we generated R noisy versions of the measure n_{I_j}, $j \in [1, R]$ with n_{I_j} identically and independently distributed according to a Poisson probability distribution of parameter I (i.e., $P_{n_{I_j}}(n_{I_j}) = e^{-I} I^{n_{I_j}} / n_{I_j}!$). Poisson noise being multiplicative, the SNR of the simulated acquisition is controlled by the value of the total intensity of the input light S_0.

In summary, the simulation results reported below will compare the performance of various sensing matrices W over a set of $M = 10^3$ distinct input Stokes vectors, each of them requiring $N = 96$ intensity measurements to be estimated, each estimation being repeated itself over $R = 10^3$ noise realizations.

4.2. Mathematical performance descriptors

In the following, we may resort to two definitions of performance metrics for the estimation problem at stakes, to account respectively on the accuracy and precision of the estimation method.

4.2.1. Accuracy

For given input Stokes vector, the accuracy of the estimation is evaluated through the computation of an average relative systematic bias $\widehat{b}$, defined by

$$\widehat{b} = \frac{\left\| \mathbf{S}_{sim} - \langle \widehat{\mathbf{S}} \rangle \right\|}{\|\mathbf{S}_{sim}\|}, \tag{8}$$

where the known simulated Stokes vector $\mathbf{S}_{sim}$ is compared to the mean estimated Stokes vector $\langle \widehat{\mathbf{S}} \rangle$ resulting from the $R = 10^3$ noise realizations for each input Stokes vector.

A further averaging over the $M = 10^3$ distinct input Stokes vectors finally allows the average bias $\langle \widehat{b} \rangle$ to be computed. This quantity will be used in the following as a global figure of merit of the estimation accuracy for the different matrices W.

4.2.2. Precision

Similarly, we proposed to evaluate the relative precision of the Stokes vector estimate by computing the norm of the vector of standard deviations of the Stokes vector components, evaluated over the $R = 10^3$ noise realizations, and normalized by the norm of the average Stokes vector estimate:

$$\widehat{\sigma} = \frac{\left\| \sqrt{\left\langle \widehat{\mathbf{S}}^2 \right\rangle - \left\langle \widehat{\mathbf{S}} \right\rangle^2} \right\|}{\left\| \left\langle \widehat{\mathbf{S}} \right\rangle \right\|}. \tag{9}$$

A further averaging over the $M = 10^3$ distinct input Stokes vectors finally allows the average relative precision $\langle \widehat{\sigma} \rangle$ to be computed. This quantity will be used in the following as a global figure of merit of the estimation precision for the different matrices W.

4.2.3. Graphical representation

In the following graphs, these descriptors $\widehat{b}$ and $\widehat{\sigma}$ will be represented in the form of a Turkey box indicating the distribution of the data in the form of quartiles (first and third quartiles), with the median represented by a red line, and the minimum and maximum value of the sample given by the vertical error bar. In addition, the mean values $\langle \widehat{b} \rangle$ or $\langle \widehat{\sigma} \rangle$ over the $M = 10^3$ various input Stokes vectors will also be represented with a pink square, as shown in Fig 4.b for instance.

4.3. Simulation results and analysis

In this subsection, we focus on the influence of the main experimental errors present on a polarimetric imaging system, such as the measurement noise, presence of partial depolarization, and finally a misalignment or a calibration error of the PSA.

4.3.1. Influence of the SNR

To estimate the influence of the SNR on the estimation of the Stokes vector, we generated similar simulations for three average intensities corresponding to 10^3, 10^4 and 10^5 photons for a fixed exposure time, leading respectively to SNR values of 31.6, 100 and 316.2. The results shown below, intending to compare the 5 different matrices W for the estimation of the Stokes vector, have been carried out on the same set of simulated measurements.

The simulation results in terms of estimation accuracy are displayed in Fig. 4, for the various SNRs and matrices W studied. As expected, the relative average bias $\langle \widehat{b} \rangle$ decreases as the SNR increases, as can be clearly seen in Fig. 4.a. On the one hand, we observe that the accuracy is clearly improved at low SNR (Fig. 4.b) when the "Tetrahedron", "Spiral" and "Spiral of Tetrahedrons" analysis matrices are considered: the mean bias is lower, but also the maximum bias observed is clearly diminished by a factor of about 3. This is interesting in the context of our study of polarimetry of highly resolved speckle grains, as the SNR will be severely degraded in low-intensity regions.

On the one hand, at high SNR (Fig. 4.d) the relative average bias seems almost similar for the various analysis matrices. However, if we look at the distribution of estimated biases, the dispersion of the biases appears to be slightly lower for the "Spiral" and "Spiral of Tetrahedrons" matrices. This lower bias dispersion seems to indicate that an analysis matrix with many states distributed uniformly over the Poincaré's sphere can provide a systematic bias that is less dependent on the polarimetric state to be analyzed, than with a matrix W comprising only a few probed states.

We now focus on the estimation precision of the different analysis matrices, which is evaluated through the computation of the normalized standard deviation of the vector estimates as in Eq. (9). As shown in Fig. 5 a., the precision logically increases with the SNR value. We also observe that

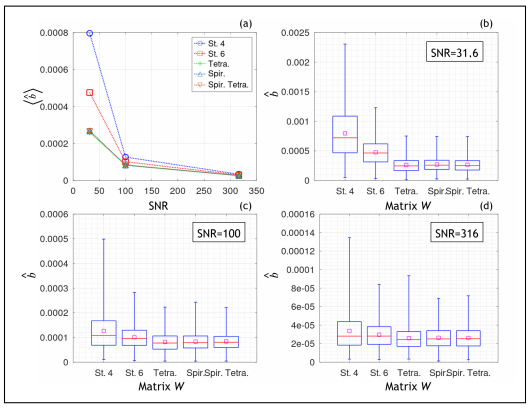

Fig. 4. (a) Average estimation bias over 1000 random polarimetric input states as a function of the SNR and for different analysis matrices W. (b-d) Distribution of the relative estimation bias over the $M = 10^3$ different polarization states, as a function of different analysis matrices for three distinct SNRs.

for a given SNR, the mean relative precision $\langle\widehat{\sigma}\rangle$ remains of the same order of magnitude for the various matrices W. More interesting to analyze is the dispersion of $\widehat{\sigma}$ over the $M = 10^3$ input states. We can clearly see that the span of values reached by the estimated relative standard deviation $\widehat{\sigma}$ is 11 times (respectively 2.75 times) higher for the *Stokes-4* approach (respectively for the *Stokes-6* approach) than for the last three matrices W, which seem to be a much better choice to avoid extreme values of standard deviations when the input Stokes vector is varied.

In order to compare the relative performances of these last three approaches, two of them being by construction optimal as they reach the minimum CN of the matrix W (*Tetrahedron* and *Spiral of Tetrahedrons*), we plot in Fig. 5.b the distribution of their relative standard deviations $\widehat{\sigma}$, for a SNR of 100. It can be seen that precision obtained for each matrix is very similar (a feature that occurred to be independent of the SNR, as tested during further simulations which are not reported here for the sake of conciseness). As discussed later, the non-optimality of the *Spiral* set of sensing states cannot be detected here, due to the important number of states $N = 96$ considered.

As an intermediate conclusion, these first simulation results confirm that the SOPAFP approaches (using either *Spiral* and *Spiral of tetrahedrons* matrix) can be employed to determine any Stokes vector with a better accuracy than usual Stokes imaging approaches, in particular at low SNR. In addition, these matrices have the supplementary advantage of providing near-optimal estimation precision, with a much lower dispersion of the estimation standard deviation compared with the more conventional *Stokes-4* and *Stokes-6* measurement methods.

4.3.2. Influence of depolarization

In this subsection, we analyze the influence of a possibly non unitary DOP of the input Stokes vector to estimate. This is common in the context of applications of polarization imaging in the biomedical or industrial field, but this can also be relevant in our context of speckle grains polarimetry. Indeed, depending on the polarization properties of the illumination light source, the DOP within a speckle grain can range from 0 to 1 in the general case. Therefore, we analyzed the robustness of the various sensing matrices W to a partial depolarization of the input Stokes vector. To this end, we simulated three different experiments, strictly similar to each other, except for the DOP p of the simulated input Stokes vector, that was varied among $p \in \{1, 0.5, 0.1\}$. This is easily operated by forming, for each normalized Stokes vector $\mathbf{s}_{in}$ generated, the following

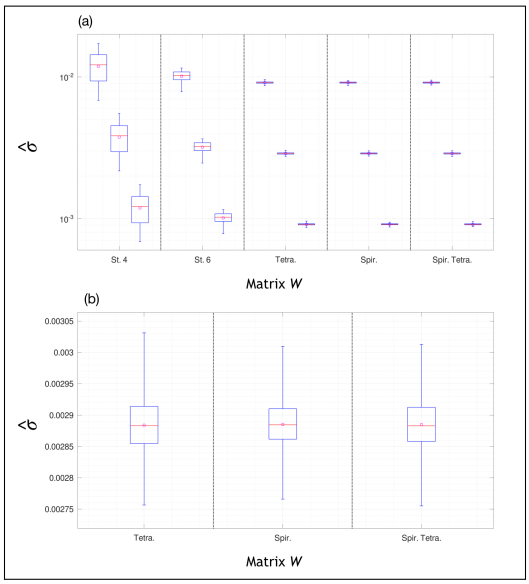

Fig. 5. (a) Influence of the SNR on the relative precision of the Stokes vector estimates for various analysis matrices W. For each analysis matrix, the three candlesticks positioned from left to right correspond respectively to SNR levels of: 31.6, 100 and 316. (b) Dispersion of the precision $\widehat{\sigma}$ of the Stokes vector estimates for the *Tetrahedron*, *Spiral* and *Spiral of Tetrahedrons* analysis matrices for a SNR of 100.

Stokes vector: $S_{in}^T = s_0 \begin{bmatrix} 1 & p \frac{\mathbf{s_{in}}^T}{\|\mathbf{s_{in}}\|} \end{bmatrix}$.

Photon noise with a SNR of 100 was again applied to the simulated signals and $R = 10^3$ realizations of noise were carried out for each of the $M = 10^3$ random states to be estimated. Concerning the estimation accuracy, Fig. 6 shows that the average relative bias increases as the DOP decreases, in a similar way for all the analysis matrices studied. To be more quantitative, we note that the ratio between the average relative bias obtained for a DOP of 1 and that of 0.1 is of the order of 10.

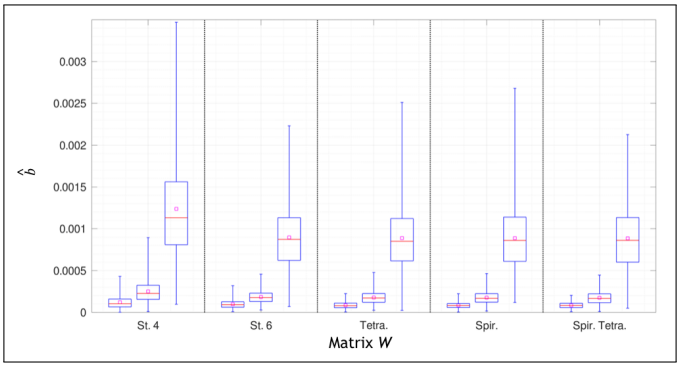

Fig. 6. Influence of the DOP of the input Stokes vector on the estimation quality of each analysis matrix. For the same analysis matrix, the three candlesticks positioned from left to right correspond respectively to a DOP of 1, 0.5 and 0.1. These simulations were carried out with an SNR of 100 and over $M = 10^3$ distinct input Stokes vectors.

Furthermore, for a given DOP, is can be observed that the average bias (pink squares) is approximately comparable, regardless of the analysis matrix chosen, except for the *Stokes-4* configuration, where the average bias obtained is 1.4 times higher than that of the other matrices. However, in terms of dispersion of the bias, Fig. 6 tends to show that for a DOP of 0.1 the *Spiral of tetrahedrons* is the best analysis matrix, the dispersion for the other matrices being slightly higher.

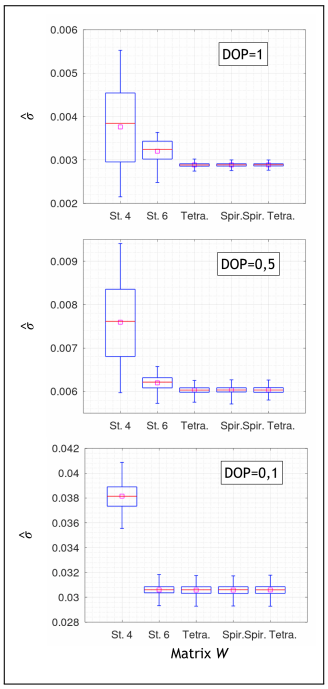

Fig. 7. Influence of depolarization on the estimation precision of the Stokes vector for each analysis matrix W. Three values of DOP are studied: 1, 0.5 and 0.1 respectively.

As for the estimation precision, Fig. 7 shows that the relative precision is degraded as the DOP decreases, by a factor of 10 between that obtained for a DOP of 1 and 0.1, independently of the analysis matrix. This ratio of precision degradation is similar to that calculated for the estimation accuracy. It can be seen that the *Tetrahedron*, *Spiral* and *Spiral of Tetrahedrons* analysis matrices have comparable accuracy (average value and dispersion) and evolve with the DOP in a similar way. The *Stokes-4* cnfiguration is still the one with the highest precision dispersion, and is therefore of little interest in our case for fine polarimetric analysis of the speckle pattern. As for the *Stokes-6* approach, the performance is lower than that of the *Tetrahedron*, *Spiral* and *Spiral of tetrahedrons* matrices for a high DOP, but as the polarization rate decreases, its precision and precision dispersion become comparable to those of the other three matrices.

Once again, the sensing configuration proposed in this artice (*Spiral of Tetrahedrons*) allows one to guarantee the best compromise between estimation accuracy and precision. This is further evidence in the next subsection, where we analyze the robustness to experimental imperfections of the setup.

4.3.3. Influence of experimental imperfections

In this section, we study the influence of a misalignment or of an incorrect calibration of one of the elements of the PSA used in the Stokes imaging setup developed to study the polarimetry of

highly resolved speckle fields. The PSA classically consists of two LCVRs ($LCVR_1$ and $LCVR_2$ respectively), whose fast axes are aligned respectively along the vertical axis and at -45° from the horizontal axis in a clockwise direction, followed by a linear polarizer along the vertical direction.

The Mueller matrix of such PSA reads $M_{PSA} = M_P(\theta_p)M_{LCVR2}(\theta_2, \phi_2)M_{LCVR1}(\theta_1, \phi_1)$ where $M_p(\theta_p)$ is the Mueller matrix of an ideal polarizer whose eigenaxis is oriented along an angle θ_p and is defined as :

$$M_P(\theta_p) = \frac{1}{2}\begin{pmatrix} 1 & c(2\theta_p) & s(2\theta_p) & 0 \\ c(2\theta_p) & c^2(2\theta_p) & c(2\theta_p)s(2\theta_p) & 0 \\ s(2\theta_p) & c(2\theta_p)s(2\theta_p) & s^2(2\theta_p) & 0 \\ 0 & 0 & 0 & 0 \end{pmatrix}, \tag{10}$$

where we set $c(x) = \cos(x)$ and $s(x) = \sin(x)$. In our case, θ_p is ideally set equal to $\pi/2$. The Mueller matrix of a variable phase plate is defined as :

$$M_{LCVR}(\theta, \phi) = \begin{pmatrix} 1 & 0 & 0 & 0 \\ 0 & c^2(2\theta) + c(\phi)s^2(2\theta) & c(2\theta)s(2\theta)\,[1 - c(\phi)] & -s(\phi)s(2\theta) \\ 0 & c(2\theta)s(2\theta)\,[1 - c(\phi)] & s^2(2\theta) + c(\phi)c^2(2\theta) & s(\phi)c(2\theta) \\ 0 & s(\phi)s(2\theta) & -s(\phi)s(2\theta) & c(\phi) \end{pmatrix}, \tag{11}$$

where θ and ϕ represent respectively the orientation of the eigenaxes and the voltage-controllable optical phase delay applied between the two propagation eigenaxes in the liquid crystal. In the ideal case, $\theta_1 = \pi/2$ and $\theta_2 = -\pi/4$.

In this section, to analyze the robustness of the estimation methods to experimental imperfections, an orientation error ϵ of 1° was introduced successively on one of the PSA elements. As described below, we also simulated a possible incorrect value of the optical phase delays due to an imperfect calibration. The analyzer Mueller matrix is thus written as :

$$M_{PSA} = M_P(\theta'_p)M_{LCVR2}(\theta'_2, \phi'_2)M_{LCVR1}(\theta'_1, \phi'_1), \tag{12}$$

with $\theta'_i = \theta_i + \epsilon_i$, $i \in \{p, 1, 2\}$, and $\phi'_i = \phi_i + \delta\phi_i$, $i \in \{1, 2\}$. For instance, simulating an orientation error in LCVR1 only will thus consists in fixing $\epsilon_1 = 1°$, and $\epsilon_2 = \epsilon_p = 0°$, $\delta\phi_i = 0$ for $i \in \{1, 2\}$. As in previous simulations, the generated signals are perturbed with photon noise corresponding to an SNR of 100, and $M = 10^3$ input Stokes vectors are tested to compute an average accuracy/precision of estimation with different analysis matrices W.

Misalignment error: We analyze in Fig. 8 the influence of a misalignment of a PSA element on the accuracy of the estimation of the Stokes vector for the various analysis matrices. The main conclusion that can be drawn from this plot is that the *Spiral* and *Spiral of Tetrahedrons* analysis matrices have a similar influence on the mean relative bias and its dispersion, regardless of which optical element of the LCVR has an orientation error. Contrarily, for the other analysis matrices, the bias introduced by an orientation error has a much higher dependency on the misoriented element, particularly if the orientation error relates to one of the variable delay plates. Thus, by probing numerous states distributed uniformly over the surface of the Poincaré's sphere, an error in the orientation of the axes of one of the PSA's optical elements will generate a bias that is comparatively low, and roughly constant irrespectively of which element is disoriented. In addition, for these two analysis matrices, the distribution of third quartiles of the estimated states is clearly lower than for other sensing strategies. These simulations thus prove that one strong

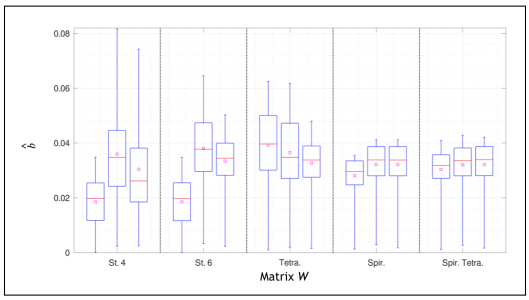

Fig. 8. Influence of a misalignment of a PSA element on the accuracy of the estimation of the Stokes vector for each analysis matrix. For each analysis matrix, the three candlesticks positioned from left to right correspond respectively to an orientation error of 1° on LCVR1, LCVR2 and polarizer.

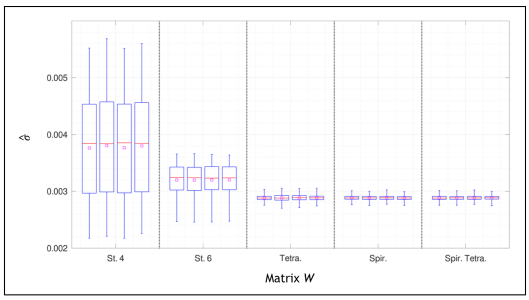

Fig. 9. Influence of a misalignment of a PSA element on the precision of the estimation of the Stokes vector for each analysis matrix. For each analysis matrix, the three candlesticks positioned from left to right correspond respectively to an orientation error of 1° on LCVR1, LCVR2 and polarizer.

interest in using the SOPAFP approach and its variants lies in its capacity to better limit the influence of experimental biases on the accuracy of the estimated results.

The precision measurement is analyzed in Fig. 9, which shows that a limited misalignment of one of the elements of the PSA has no influence on the accuracy of the estimate of the Stokes vector. This observation can be interpreted by the fact that a (limited) misalignment of the PSA simply leads to the estimation of an inaccurate (biased) polarization state. In this way, analysis matrices composed of many states distributed uniformly over the surface of the Poincaré's sphere have an rather constant bias regardless of the misaligned element (as shown above) and consequently, a less significant bias dispersion giving them greater robustness to experimental orientation errors of the optical setup.

LCVR calibration error: Another source of experimental error can be encountered when an incorrect calibration of the LCVRs voltage setpoint is used (due to an imprecise calibration, temperature drifts...). Fig. 10.a shows the calibration curve of the LCVRs used in our experiment providing the optical phase delay generated when a control voltage V is applied on the cell, at a stabilized temperature of 24° C. As mentioned in the first article of this series [1], a polynomial fit of these calibration curves allowed us to easily simulate the influence of a systematic error δV_i in the voltage setpoints, by simulating the following Mueller matrix for the PSA: .

$$M_{PSA} = M_P(\theta_p) M_{LCVR2}(\theta_2, \phi_2') M_{LCVR1}(\theta_1, \phi_1'), \tag{13}$$

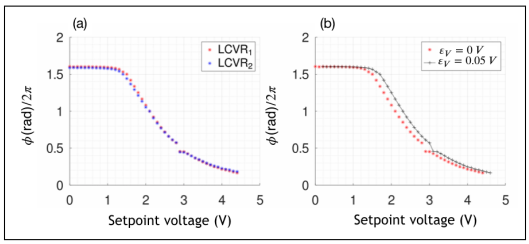

Fig. 10. (a) Calibration curve for the two LCVR plates for 45 different voltages ranging from 0 to 4.5 V, in steps of 0.1 V. (b) LCVR1 calibration curve with and without a set-point voltage error $\epsilon_V = 0.05$.

with $\phi_i' = \phi_2(V_i + \delta V_i), i \in \{1, 2\}$. An error of $\delta V_1 = 0.05$ V has been simulated and provides the erroneous response in optical phase delay shown in Fig. 10.b.

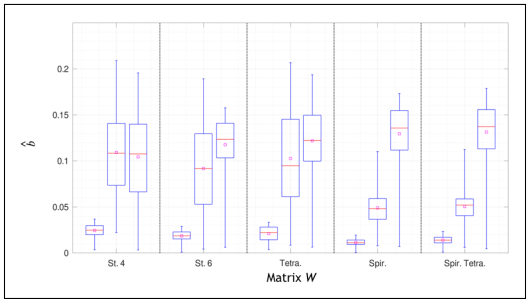

Fig. 11. Influence of a calibration error on one of the PSA variable delay plates on the accuracy of the Stokes vector estimation for each analysis matrix. For each analysis matrix, the three candlesticks positioned from left to right correspond respectively to a perfect calibration, a calibration error on LCVR1 or on LCVR2.

Figure 11 shows the influence of such an imperfect voltage calibration on the accuracy of the Stokes vector estimation. It can first be observed that the average relative bias $\langle \hat{b} \rangle$ for a voltage error on LCVR2 is higher than that for an error on LCVR1 (except for the *Stokes-4* matrix). In the case of a setpoint error on LCVR1, the average bias for the *Spiral* and *Spiral of Tetrahedrons* analysis matrices is half that of the other matrices. Furthermore, in this case they have a lower bias dispersion. However, this analysis is different if the setpoint voltage error affects LCVR2: in that case the *Spiral* and *Spiral of Tetrahedrons* analysis matrices are affected by a bias comparable to that of other sensing approaches. This difference in behaviour between the two LCVRs can be explained by looking at Eq. (5): the optical phase delay induced by LCVR2, ϕ_2, modifies three of the four terms of the equation, whereas the delay induced by LCVR1 only affects two of them.

On the other hand, an error in the setpoint voltage on one of the variable delay plates has very little effect on the average precision of each analysis matrix as shown in Fig. 12. As a result, to conclude this section, it can be again observed that for a voltage calibration error on the LCVR setpoints, the *Spiral* and *Spiral of Tetrahedrons* analysis matrices exhibit a lower dispersion than the other analysis matrices in terms of accuracy (relative bias) and precision (relative standard deviation).

5. Discussion and conclusion

The numerical simulations presented in this study have permitted to clearly validate the relevance of SOPAFP sensing approaches in Stokes polarimetry, i.e., performing polarimetric sensing

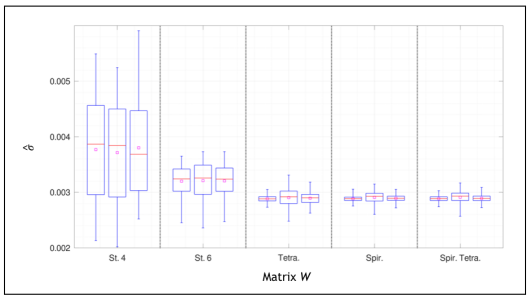

Fig. 12. Influence of a calibration error on one of the PSA variable delay plates on the precision of the determination of the Stokes vector for each analysis matrix. For each analysis matrix, the three candlesticks positioned from left to right correspond respectively to a perfect calibration, a calibration error on LCVR1 and on LCVR2.

using many (apparently superfluous) intensity measurements along a strong diversity of analysis states. Even though such approaches should be limited to particular experimental contexts where the acquisition time is not a limiting factor, the gain in estimation quality with the SOPAFP approach had already been noticed in the seminal paper of Dupont *et al.* [15], but without a clear demonstration of its origin.

In this paper, we first demonstrated that the non-linear regression procedure implemented in [15] could be advantageously replaced by a direct matrix inversion (or pseudo-inversion), with a huge acceleration of processing times by a factor of more than 1500. We then proposed an alternative set of polarization analysis states, referred to as *Spiral of Tetrahedrons*, that allows one to perform SOPAFP with an important number of sensing states covering as uniformly as possible the Poincaré's sphere, while at the same time ensuring an optimum CN of the analysis matrix to ensure optimal precision in the estimation by direct inversion.

Using extensive simulations of realistic imaging/sensing situations, we demonstrated that SOPAFP approaches involving the *Spiral* and *Spiral of Tetrahedrons* analysis matrices could provide optimal estimation accuracy (in terms of relative estimation bias) and precision whatever the SNR or DOP of the input light. More interestingly, these SOPAFP approaches were shown to clearly supersede other classical sensing strategies involving only a limited number of analysis states in the case of slight experimental imperfections of the setup, resulting from improper alignment or bad calibration of the LCVRs for instance, that can happen in practice, due to temperature drifts. Indeed, we demonstrated that the SOPAFP approaches provide a low average relative bias and, more importantly, a very low dispersion of this relative bias as a function of the input polarization state to estimate, and for distinct imperfections of the PSA.

Now, a last topic that can be discussed in this study is the effective interest of using the *Spiral of Tetrahedrons* analysis matrix we proposed instead of any kind of uniformly distributed set of points across de Poincaré's sphere. As shown in Section 3.4.2, maximal coverage of the sphere does not guarantee that the CN of the analysis matrix is minimum: therefore using a non-optimal set of points should lead to a lower estimation precision. Although this was not detected in the simulations presented above due to the important number of sensing points used ($N = 96$), we compare in a last simulated experiment the relative performance in terms of precision between the *Spiral* and *Spiral of Tetrahedrons* analysis matrices, when the number of points N is varied, and for three values of the DOP of the input Stokes vectors to estimate. The results obtained and displayed in Fig. 13 confirm the fact that the slight non-optimality of the CN of the *Spiral* analysis matrix which can be observd in Fig. 2.b) leads to a small degradation of the estimation precision with respect to the *Spiral of Tetrahedrons* analysis matrix which has an optimum CN, this degradation being more pronounced for lower DOP of the input Stokes vector. Depending

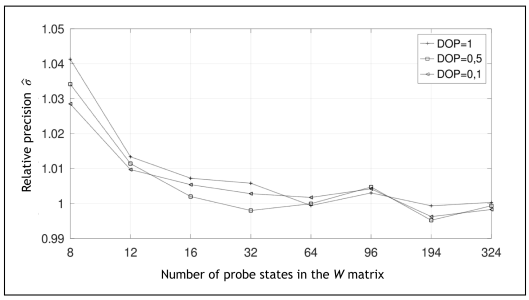

Fig. 13. Relative precision defined by the ratio of the precision of the *Spiral* and *Spiral of Tetrahedrons* analysis matrices for three levels of degree of polarization (1, 0.5 and 0.1) for W matrices composed of 8 to 324 probe states.

on the application at hand, one could choose a different compromise between acquisition time and estimation precision/robustness by diminishing slightly the number of states composing the *Spiral of Tetrahedrons*. In the context of this article series, we sticked to a number of sensing points of $N = 96$, leading in our case to acceptable acquisition times.

As a conclusion, the SOPAFP approach and the proposed optimal alternative implementation using the *Spiral of Tetrahedrons* analysis matrix can prove very efficient in applicative contexts where very good accuracy/precision of the Stokes vector estimation is required, and in particular in low SNR contexts and in the presence of depolarized input states. Moreover, we proved in this study that such approaches are optimal also in terms of robustness to experimental imperfections. As suggested in Ref. [15], the experimental challenge of performing Stokes polarimetry of highly resolved speckle patterns at the individual grain scale is a perfect context for applying SOPAFP approaches. Using the experimental setup detailed in the first article of this series [1], we shall use the optimizes SOPAFP approach in the last article of the series [19] which details some of the imaging results obtained experimentally with such optimized setup, as well as new graphical representations of the polarization information, and an analysis of the distribution of polarization states accross a speckle pattern, and in vicinity of polarization singularities.

Acknowledgments. The authors would like to thank Richard Ganaye for his relevant insight into spatial geometry. They also acknowledge the DOP team and in particular Mehdi Alouini for fruitful discussions.

Disclosures. The authors declare no conflicts of interest.

Data availability. Data underlying the results presented in this paper are not publicly available at this time but may be obtained from the authors upon reasonable request.

Supplemental document. See Supplement 1 for supporting content.

References

1. J. Staes and J. Fade, "Optimized stokes imaging for highly resolved optical speckle fields – i. optimized experimental setup," submitted to J. Opt. Soc. Am. A (2023).
2. J. Dupont and X. Orlik, "Speckle fields polarimetry: statistical analysis and polarization singularities measurements," in *SPECKLE 2015: VI International Conference on Speckle Metrology,* vol. 9660 (SPIE, 2015), pp. 259–269.
3. S. Huard, *Polarization of light* (Wiley, 1997).
4. D. H. Goldstein, *Polarized light* (CRC press, 2017).
5. N. A. Rubin, A. Zaidi, M. Juhl, R. P. Li, J. B. Mueller, R. C. Devlin, K. Leósson, and F. Capasso, "Polarization state generation and measurement with a single metasurface," Opt. Express **26**, 21455–21478 (2018).
6. J. Bai and Y. Yao, "Highly efficient anisotropic chiral plasmonic metamaterials for polarization conversion and detection," ACS Nano **15**, 14263–14274 (2021).

7. J. Zuo, J. Bai, S. Choi, A. Basiri, X. Chen, C. Wang, and Y. Yao, "Chip-integrated metasurface full-stokes polarimetric imaging sensor," Light. Sci. & Appl. **12**, 218 (2023).
8. R. Azzam, I. Elminyawi, and A. El-Saba, "General analysis and optimization of the four-detector photopolarimeter," JOSA A **5**, 681–689 (1988).
9. D. Sabatke, M. Descour, E. Dereniak, W. Sweatt, S. Kemme, and G. Phipps, "Optimization of retardance for a complete stokes polarimeter," Opt. Lett. **25**, 802–804 (2000).
10. J. S. Tyo, D. L. Goldstein, D. B. Chenault, and J. A. Shaw, "Review of passive imaging polarimetry for remote sensing applications," Appl. optics **45**, 5453–5469 (2006).
11. J. S. Tyo, "Design of optimal polarimeters: maximization of signal-to-noise ratio and minimization of systematic error," Appl. optics **41**, 619–630 (2002).
12. F. Goudail, "Noise minimization and equalization for stokes polarimeters in the presence of signal-dependent poisson shot noise," Opt. letters **34**, 647–649 (2009).
13. F. Goudail, "Equalized estimation of stokes parameters in the presence of poisson noise for any number of polarization analysis states," Opt. letters **41**, 5772–5775 (2016).
14. A. Ling, K. P. Soh, A. Lamas-Linares, and C. Kurtsiefer, "Experimental polarization state tomography using optimal polarimeters," Phys. Rev. A **74**, 022309 (2006).
15. J. Dupont, X. Orlik, A. Ghabbach, M. Zerrad, G. Soriano, and C. Amra, "Polarization analysis of speckle field below its transverse correlation width: application to surface and bulk scattering," Opt. Express **22**, 24133–24141 (2014).
16. G. Dahlquist and Å. Björck, *Numerical methods in scientific computing, volume I* (SIAM, 2008).
17. G. octave, "fminsearch()." https://octave.sourceforge.io/octave/function/fminsearch.html. Accessed 2023-12-12.
18. J. A. Nelder and R. Mead, "A simplex method for function minimization," The computer journal **7**, 308–313 (1965).
19. J. Staes and J. Fade, "Optimized stokes imaging for highly resolved optical speckle fields – iii. optimized polarimetric data representation & topological polarimetric analysis," submitted to J. Opt. Soc. Am. A (2023).
20. E. B. Saff and A. B. Kuijlaars, "Distributing many points on a sphere," The mathematical intelligencer **19**, 5–11 (1997).
21. C. Carlson, https://blog.wolfram.com/2011/07/28/how-i-made-wine-glasses-from-sunflowers/. Accessed: 2023-12-12.